China Ocean Eng., 2020, Vol. 34, No. 3, P. 441–449
DOI: https://doi.org/10.1007/s13344-020-0040-6, ISSN 0890-5487
http://www.chinaoceanengin.cn/ E-mail: coe@nhri.cn

Accumulated Rotation of A Modified Suction Caisson and Soil Deformation Induced by Cyclic Loading

BAI Yun[a], LI Da-yong[a, b, *], ZHANG Yu-kun[a]

[a] Key Laboratory of Civil Engineering Disaster Prevention and Mitigation, Shandong University of Science and Technology, Qingdao 266590, China

[b] College of Civil Engineering, Fuzhou University, Fuzhou, Fujian 350108, China

Received February 19, 2019; revised February 28, 2020; accepted April 2, 2020

Abstract

Modified suction caissons (MSCs) acting as offshore wind turbine foundations will generate the accumulated rotation under cyclic loading resulted from waves. The accumulated rotation and the range of soil deformation around the MSC under long-term cyclic wave loading were studied using 3-D numerical simulations. The Morison equation was adopted to calculate the wave loadings. It was found that the MSC accumulated rotation increases linearly with the increase of the logarithm of cyclic number. The normalized expression was proposed to reflect the relationship between the accumulated rotation and cyclic number. The soil deformation range around the MSC increases when increasing the cyclic number and loading amplitude. It can also be concluded that the accumulated rotation increases rapidly with this change of excess pore pressure in the first 4000 cycles. The responses of the MSC to wave and wind loads were also investigated. Results show that the accumulated rotation of the MSC under both wave and wind loadings is larger than that under the wave loading only.

Key words: modified suction caisson (MSC), wave loading, accumulated rotation, soil deformation range

Citation: Bai, Y., Li, D. Y., Zhang, Y. K., 2020. Accumulated rotation of a modified suction caisson and soil deformation induced by cyclic loading. China Ocean Eng., 34(3): 441–449, doi: https://doi.org/10.1007/s13344-020-0040-6

1 Introduction

The offshore wind power has drawn more attention as it has no CO_2 emission, no pollution and is highly economical (Dean, 2010). An offshore wind turbine (OWT) foundation suffers from both the vertical loading transmitted from self-weight of superstructures and environmental lateral cyclic wave and wind loadings (Awad-Allah et al., 2017; Liu et al., 2019). Lateral cyclic loads have greater influence on the OWT foundation over the vertical load, which leads to the accumulation rotation and the soil deformation around the foundation. According to China Design Code FD003-2007 (Hydropower and Water Resources Planning and Design General Institute, 2008), the OWT foundation accumulation rotation angle is strictly limited within 0.17°. Thus, it is of importance to study the accumulated rotation behavior of the OWT foundation induced by cyclic loading to guide the foundation design.

The suction caisson has been regarded as an alternative to a monopile for the OWT, which can be used in various water depths (Senders, 2009). In order to increase the foundation bearing capacity and to reduce the accumulation rotation, the modified suction caisson (MSC) has been proposed (Fig. 1), adding an external short-circular structure. A series of experimental studies and numerical simulations have been conducted on the MSC and the related results show that the MSC can be installed in dense sand and clay to the required depth by the combination of suction and self-weight. In addition, the ultimate bearing capacity of the MSC is larger than that of the regular suction caisson (RSC) (Zhang et al., 2016; Li et al., 2015). Furthermore, Li et al. (2017) carried out a series of numerical simulations on the combined bearing behavior of MSCs and RSCs under the equal steel mass. It is proven that the bearing capacity of MSC is larger than that of the RSC under the same mass. However, it is necessary to understand the MSC cyclic bearing behavior and accumulated rotation under long-term lateral cyclic loading.

Some ideas from the RSC or piles can be used to study the response of the MSC to long-term cyclic loadings. Nielsen et al. (2017) conducted model test to study the influence of the cyclic loading with the frequency of 1.0 Hz on the mono suction caisson embedded in dense sand and

Foundation item: This research is financially supported by the National Natural Science Foundation of China (Grant Nos. 51639002, 51879044 and 51808325) and SDUST (Shandong University of Science and Technology) Research Fund (Grant No. 2015KYTD104).
*Corresponding author. E-mail: ldydy@163.com

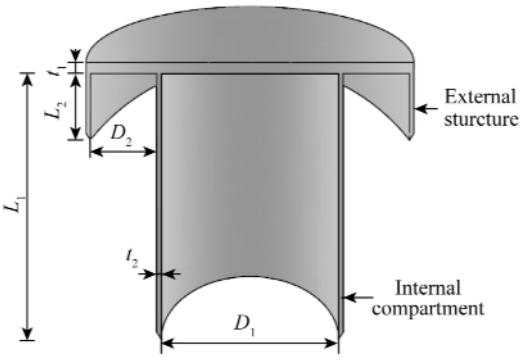

Fig. 1. Sketch of the MSC.

found that the two-way loading leads to the largest rotation of the foundation. Zhu et al. (2013) carried out experimental research on suction caisson in dry sand to obtain the bearing behavior under long-term loading under the fully drained condition. The suction caisson settlement increases with the increasing of the cyclic number and the cyclic amplitude. In addition, Yang et al. (2018) proposed the degradation stiffness model (DSM) to reflect the soil strength degradation under long-term cyclic loading. They also proposed a method of calculating the accumulated displacement of the laterally loaded pile by considering the effects of the cyclic number, embedded depth of pile and load amplitude. Nikitas et al. (2016) presented a simple loading device that can apply millions of cycle loadings to estimate the long-term performance of the pile, and the device also takes the influence of wind and wave loadings into consideration.

The bearing behavior of the MSC during long-term cyclic wave loading was investigated with PLAXIS-3D software. The influence factors of cyclic number, cyclic amplitude, and loading character on the accumulated rotation of MSC were discussed. The range of the soil deformation around the MSC was also obtained. The accumulated rotation of the MSC under the combination of the wave load and wind loads was also studied. Further, an expression was obtained to calculate the MSC accumulated rotation.

2 Numerical modeling

2.1 Finite element model

The regular suction caisson foundation (RSC) for the Vestas V90-3.0 MW wind turbine in the Frederikshavn wind farm in Denmark was used in this study (Ibsen and Brincker, 2004). The dimensions of the RSC and the corresponding MSC are given in Table 1. It should be noted that the self-weight of the MSC equals that of the mono suction caisson. The wind turbine tower is 80 m high and self-weight of the upper structure equals 1290 kN.

Table 1 Dimensions of Suction Caissons

	D_1 (m)	L_1 (m)	D_2 (m)	L_2 (m)	t_1 (m)	t_2 (m)
Regular suction caisson	6	18	–	–	0.3	0.1
Modified suction caisson	6	12	2	2		

2.2 UBC3D-PLM constitutive model

A novel constitutive relationship, UBC3D-PLM (Tsegaye, 2010), was used for modelling the sand, which can simulate the behavior of sand under cyclic and dynamic loadings. In addition, it can reproduce the excess pore water pressure accumulation and soil densification under cyclic loading (Galavi et al., 2013). An introduction to the UBC3D-PLM constitutive relationship is depicted as follows (Ju et al., 2016; Wobbes et al., 2017).

2.2.1 *Yield surface*

The critical yield surface defined by the Mohr-Coulomb function is expressed by

$$f_{\mathrm{m}}=\frac{1}{2}\left(\sigma'_{\max}-\sigma'_{\min}\right)-\left[\frac{1}{2}\left(\sigma'_{\max}-+\sigma'_{\min}\right)+c\cot\varphi_{\mathrm{p}}\right]\sin\varphi_{\mathrm{mob}}, \tag{1}$$

where f_{m} represents the yield function expression, $\sigma'_{\max}$ and $\sigma'_{\min}$ represent the maximum and minimum principal stress, respectively; φ_{p} is the pear value of the soil friction angle; φ_{mob} is the mobilized friction angle during hardening; c is cohesion.

2.2.2 *Elasto-plastic behavior and hardening rule*

An isotropic, non-linear law is given in terms of the elastic shear modulus (G) and the elastic bulk modulus (K).

$$\begin{cases}K=k_B^{*e}p_{\mathrm{ref}}\left(\dfrac{p}{p_{\mathrm{ref}}}\right)^{me}\\ G=k_G^{*e}p_{\mathrm{ref}}\left(\dfrac{p}{p_{\mathrm{ref}}}\right)^{ne}\end{cases} \tag{2}$$

where p is the mean effective stress; p_{ref} is the reference stress; k_B^{*e} and k_G^{*e} represent the bulk and shear modulus, respectively, which are input parameters; *me* and *ne* define the rate of stiffness.

The hardening rule formulated by Tsegaye (2010), connecting the increment of sine of mobilized friction angle φ_{mob} with the plastic strain increment, is given as:

$$\mathrm{d}\sin\varphi_{\mathrm{mob}}=1.5k_G^{*p}\left(\frac{p}{p_{\mathrm{ref}}}\right)^{np}\frac{p_{\mathrm{ref}}}{p_{\mathrm{m}}}\left(1-\frac{\sin\varphi_{\mathrm{mob}}}{\sin\varphi_{\mathrm{p}}}R_{\mathrm{f}}\right)^2\mathrm{d}\lambda, \tag{3}$$

where $\mathrm{d}\sin\varphi_{\mathrm{mob}}$ is the increment of the sine of mobilized friction angle, $\mathrm{d}\lambda$ represents increment multiplier of the plastic strain, R_{f} is the failure ratio, and p_{m} is equal to $(\sigma'_1+\sigma'_3)/2$.

The shear modulus factor k_G^{*p} is the function of the cycle number used as an input parameter during first time loading. During secondary loading, it can be obtained by

$$k_{G\mathrm{secondary}}^{*p}=k_G^{*p}\left(4+\frac{n_{\mathrm{rev}}}{2}\right)hard\cdot f_{\mathrm{dens}}, \tag{4}$$

where n_{rev} is the shear stress number; *hard* is the factor required to correct the densification rule; f_{dens} is the densifica-

tion factor.

2.2.3 *Soil degradation*

The stiffness degradation of sand caused by post-liquefaction is formulated based on the plastic deviatoric strain related to the dilation of the soil. This leads to the soil stiffness degradation during contraction after unloading. The stiffness degradation law can be expressed as

$$k^{*p}_{G\text{post-liquefaction}} = k^{*p}_{G} E_{\text{dil}}; \tag{5}$$

$$E_{\text{dil}} = \max\left(e^{-110\varepsilon_{\text{dil}}}; f_{\text{Epost}}\right), \tag{6}$$

where $k^{*p}_{G\text{post-liquefaction}}$ is the plastic shear modulus factor during liquefaction, ε_{dil} is the accumulation of the plastic deviatoric strain generated during dilation of soil, and f_{Epost} is the parameter to adjust post-liquefaction behavior.

2.2.4 *Determination of parameters in the UBC3D-PLM*

In this study, the marine fine sand with the particle size range of 0.075−0.3 mm was collected from Qingdao sea region. The particle size distribution curve and physical parameters of the sand were obtained by Li et al. (2015). The relative density D_{r} equals 0.75 and internal friction angle φ_{cv} equals 20° which were obtained from laboratory tests. The seepage coefficient of sand k=0.0825 mm/s and was calculated by using empirical equations in the PLAXIS software. In order to obtain more accurate results, the seepage coefficient and the void ratio will be also obtained by doing laboratory tests in further studies. The parameters of sand are listed in Table 2.

Table 2 Parameters of sand

Parameter	Value
Relative density D_{r}	0.75
Elastic bulk modulus factor k^{*e}_{B}	920
Elastic shear modulus factor k^{*e}_{G}	1314
Plastic shear modulus factor k^{*p}_{G}	946
Elastic bulk modulus index *me*	0.5
Elastic shear modulus index *ne*	0.5
Plastic shear modulus index *np*	0.4
Reference pressure p_{ref} (kPa)	100
Constant volume friction angle φ_{cv} (°)	20
Peak friction angle φ_{p} (°)	24.5
Cohesion c (kPa)	0

2.3 Wave load calculation

The water depth is considered in this study to be 10 m, the height (H) and period (T) of the wave are 3 m and 10 s, respectively. Therefore, the corresponding wave length, L_{wave}, equals 75.9 m. The simplified wave load is calculated by using Morison equation (Morison et al., 1950; Arany et al., 2017), and the methodology is in terms of the Stokes third-order theory.

$$\eta = \frac{1}{k}\sum_{n=1}^{5}\lambda_n \cos\left[n(kx-\omega t)\right]; \tag{7}$$

$$u_x = \frac{\partial \Phi}{\partial x} = c\sum_{n=1}^{5} n\lambda_n \cosh\left[nk(z+h_w)\right]\cos\left[n(kx-\omega t)\right]; \tag{8}$$

$$a_x = \frac{\partial u_x}{\partial t} = \omega c\sum_{n=1}^{5} n^2\lambda_n \cosh\left[nk(z+h_{\text{w}})\right]\sin\left[n(kx-\omega t)\right], \tag{9}$$

where η is the surface elevation, u_x is the horizontal particle velocity, a_x is the horizontal particle acceleration. In addition, the wave number k equals $2\pi/L_{\text{wave}}$, the wave velocity c equals L_{wave}/T, λ_n is the coefficient determined by wave number k and water depth h_{w}.

The wave load can be expressed as:

$$F_H = \int_0^{h_{\text{w}}} \frac{1}{2} C_{\text{D}} \rho D u_x |u_x| \,\text{d}z + \int_0^{h_{\text{w}}} \frac{1}{2} C_{\text{M}} \rho \frac{\pi D^2}{4} \frac{\partial u_x}{\partial t} \,\text{d}z, \tag{10}$$

where the density of seawater ρ=1.02 kg/m^3, C_{D} is the coefficient of drag, C_{M} is the coefficient of mass. According to China Classification Society (2005), the coefficient C_{D} ranges from 0.6 to 1.2, and C_{M} ranges from 1.3 to 2.0. It defines C_{D}=1.2, C_{M}=2.0 in this study.

The wave load calculated by the Morrison equation is applied in the position of 5 m above the caisson lid. Fig. 2 shows 10 cycles of horizontal wave load.

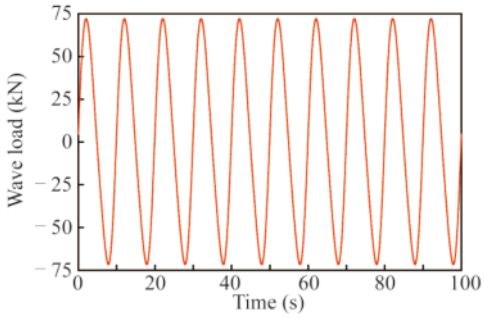

Fig. 2. Wave load−time period curve.

2.4 Procedures of numerical simulation

The 10-node tetrahedral elements were used for sand. The sand domain dimensions are 10D in width and 5H in height to avoid boundary effects. Displacements at the bottom boundary are fully fixed and horizontally fixed at the lateral boundaries. The viscous option of the dynamic boundary condition was used to simulate the far-field behavior by absorbing the increment of stresses caused by cyclic loading spurious wave reflection inside the soil. The suction caisson-sand interface was simulated by using interface elements.

The numerical modeling is conducted in three steps. The first step is an initial stress generation step by using the K_0 procedure. Then the suction caisson is installed to the desire depth. In the last step, the cyclic response of suction caisson to the long-term wave loading is analyzed.

3 Accumulated rotation of suction caissons under wave loading

3.1 Accumulated deflection of suction caissons

Fig. 3 gives the deflection-cyclic number relationships of the RSC and the MSC in the first 100 cycles. It can be found that the deflections of suction caissons vary with the direction of wave load, and the accumulated deflection is generated after each cycle. The deflection of the MSC decreases by approximately 21% compared with the RSC, indicating that the MSC is capable of limiting the deflection under wave loading.

3.2 Accumulated rotation and soil deformation around the MSC

As shown in Fig. 4, the accumulated rotation of suction caisson increases obviously with the increasing cyclic cycle. When the loading cycle value exceeds 4000, the accumulated angular rotation value tends to be stable gradually. It can also be found that the MSC can effectively limit the accumulated rotation compared with the RSC under the equal steel mass.

The range of the deformed soil around the MSC under various load cycles is given in Fig. 5. The deformed soil region increases with the increase of the loading cyclic number. As a result, the accumulated rotation of the MSC and subsidence in the vertical direction are produced.

During cyclic loading, the excess pore water pressure around the suction caisson increases and the effective stress decreases simultaneously, leading to the soil strength degradation. Therefore, the accumulated rotation of the suction caisson occurs. Fig. 6 gives the excess pore pressure variations in sand inside and outside the internal structure of the MSC during cyclic loading. The excess pore pressure in sand inside the internal structure first increases with the in-

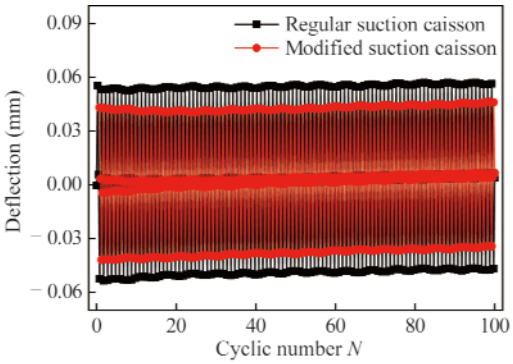

Fig. 3. Deflection of suction caissons under wave load.

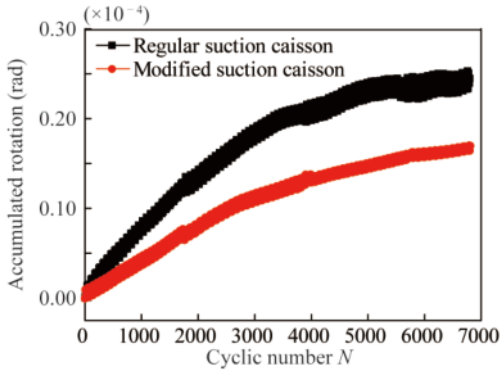

Fig. 4. Rotation of the MSC under wave load.

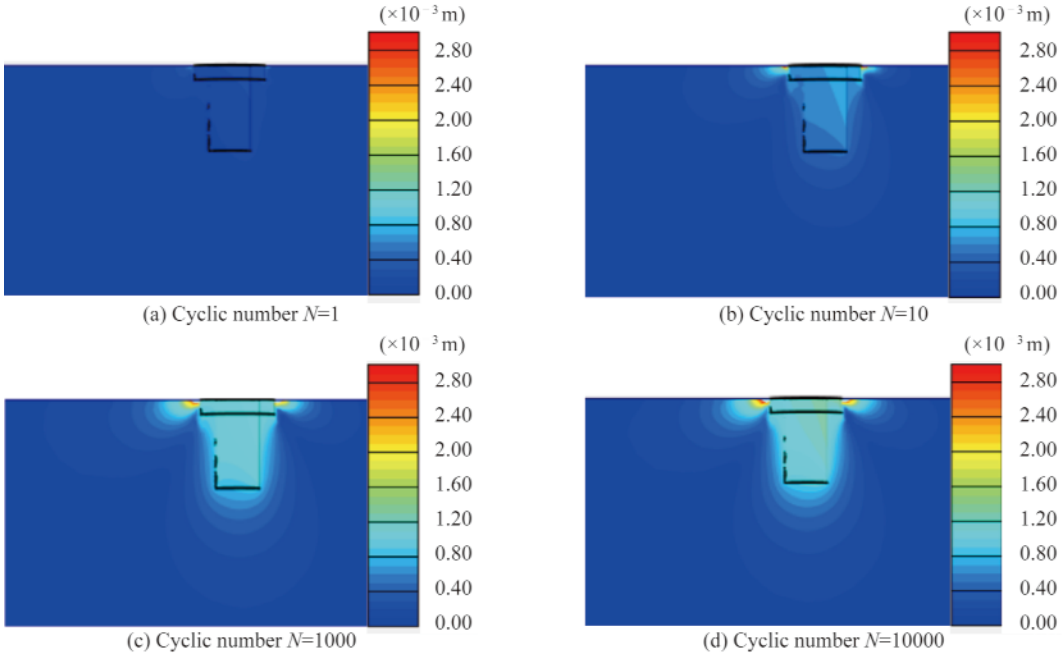

Fig. 5. Displacement contours of the MSC under wave load.

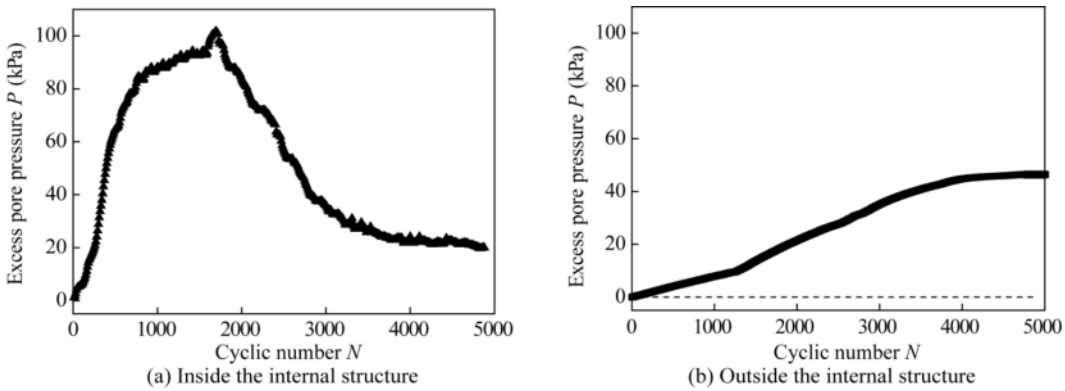

Fig. 6. Excess pore pressure variations in sand inside and outside the MSC.

creasing of the cyclic cycles to the maximum value, then decreases sharply. On the contrary, the excess pore pressure in sand outside the internal structure increases with the increasing cyclic cycles. The excess pore pressure tends to be stable when the cyclic cycle value reaches 4000. It can be concluded that the accumulated rotation increases rapidly with the change of excess pore pressure in the first 4000 cycles. As the excess pore pressures inside and outside the internal structure trend to be stable, the increase of accumulated rotation appears to have stabilized, as shown in Fig. 4.

4 Effect of waveform parameters on accumulated rotation of MSC

4.1 Cyclic bearing behavior of MSC

In reality, most of wind turbines are installed in shallow water, which are mainly subjected to asymmetrical sinusoidal cyclic loadings. Leblanc et al. (2010) has proposed two independent parameters to define the asymmetrical sinusoidal cyclic loadings:

$$\xi_b = \frac{F_{\max}}{F_{\text{ult}}},\ \xi_c = \frac{F_{\min}}{F_{\max}}, \tag{11}$$

where $F_{\max}$ and $F_{\min}$ are the maximum and minimum loads in each load cycle, and F_{ult} is the monotonic MSC ultimate bearing capacity and can be obtained from Fig. 7. In this study, the ultimate bearing capacity is reached when the MSC deflection reaches 0.1 times the diameter of the internal compartment.

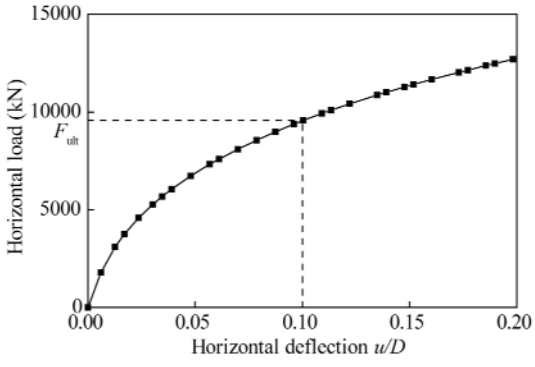

Fig. 7. Load−displacement curve for the MSC.

The dimensionless parameter ξ_c donates the loading type (Fig. 8); −1 is for two-way symmetrical loading, and 0 is for one-way loading. The parameter ξ_b represents the load amplitude, typically ranging from 0.1 to 0.5. The simulate program addresses the range of ξ_c and ξ_b to analyze the MSC accumulated rotation.

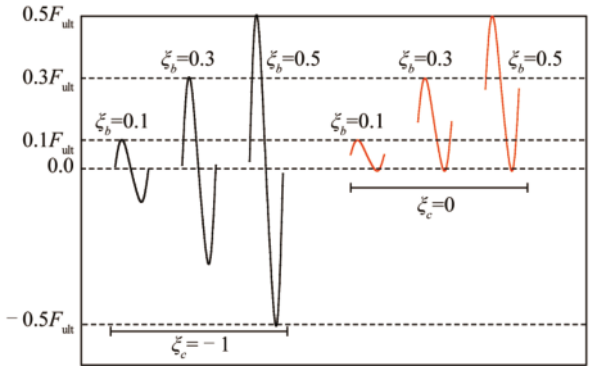

Fig. 8. Cyclic parameters ξ_b and ξ_c.

4.2 Effects of ξ_b and ξ_c on the accumulated rotation of the MSC

Fig. 9 gives the relationships between the accumulated rotation and cyclic number of the MSC under different ξ_b and ξ_c values. It can be concluded from the curves that an increasing load amplitude will lead an increase in the accumulated rotation. And the accumulated rotation increases obviously in the first 4000 cycles. By comparing Fig. 9a with Fig. 9b, it can be found that the one-way loading leads to larger rotations of the MSC than the two-way loading.

Fig. 10 represents the relationship between the accumulated rotation and the cyclic number in logarithmic form. The accumulated rotation ($\Delta\theta(N)$) of MSC follows a linear relationship with the logarithm of the number of cycles. The relationship can be expressed as

$$\Delta\theta(N) = a + b\lg N, \tag{12}$$

where the accumulated rotation $\Delta\theta(N) = (\theta_N - \theta_1)/\theta_s$; θ_1

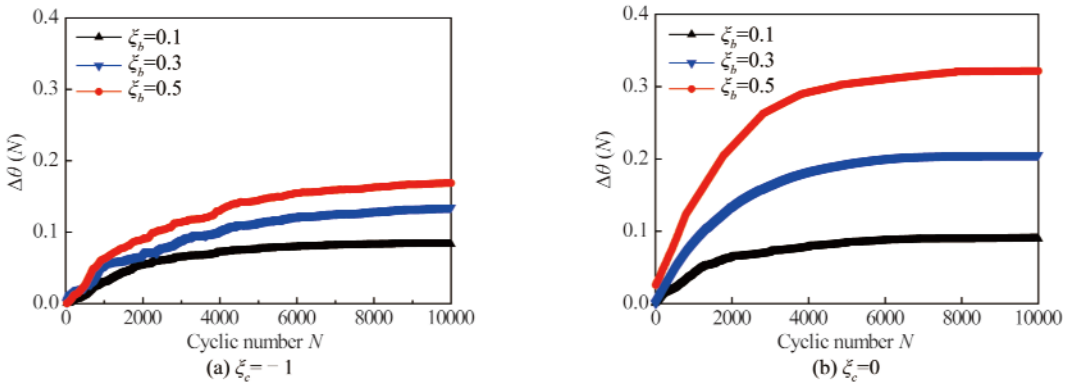

Fig. 9. Rotation in relation to cycles under various ξ_b.

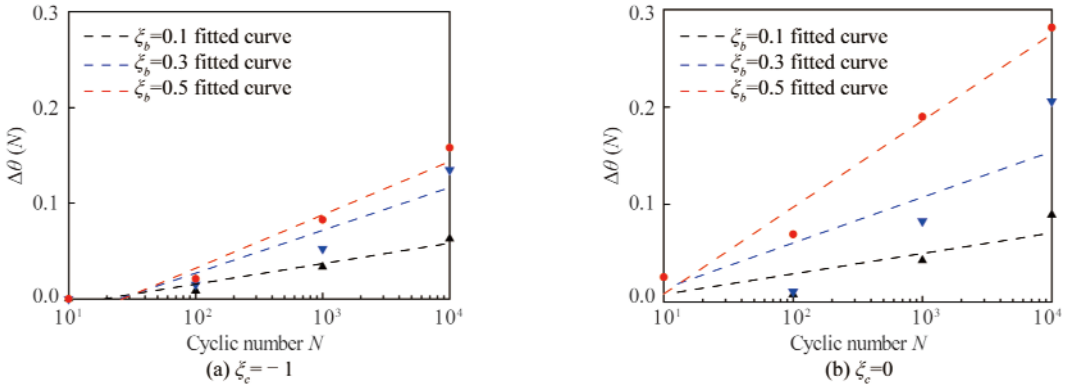

Fig. 10. Relationships between lg$N$ and accumulated rotation.

and θ_N represent the rotation of the MSC after the first load cycle and N load cycles, respectively; θ_s is the rotation when the MSC reaches its ultimate state; N is the number of cycles. As shown in Fig. 11, coefficient a decreases with the increase of ξ_b while coefficient b increases. It can be concluded that a higher rate of rotation accumulating can be obtained under larger load amplitude. It can also be obtained from Fig. 11 that coefficients a and b in Eq. (12) range from −0.1 to 0 and 0 to 0.1, respectively. It is possible to predict the accumulated rotation of the MSC after a certain load cycle by using Eq. (12).

It should be noticed from Fig. 12 that the vertical settlement of the MSC occurs under cyclic loading. The settlement was found to increase with the increasing magnitude of ξ_b. In the initial stage of loading, the MSC subsides rapidly due to its self-weight, and then the vertical settling rate decreases with the increasing cyclic number, eventually attaining a critical value. The above phenomenon could be explained as follows: with the increase of cyclic number, the soil gradually becomes denser, or a part of the sand is squeezed to the outside, resulting in the settlement of the MSC. It was also found that the increase of load amplitude

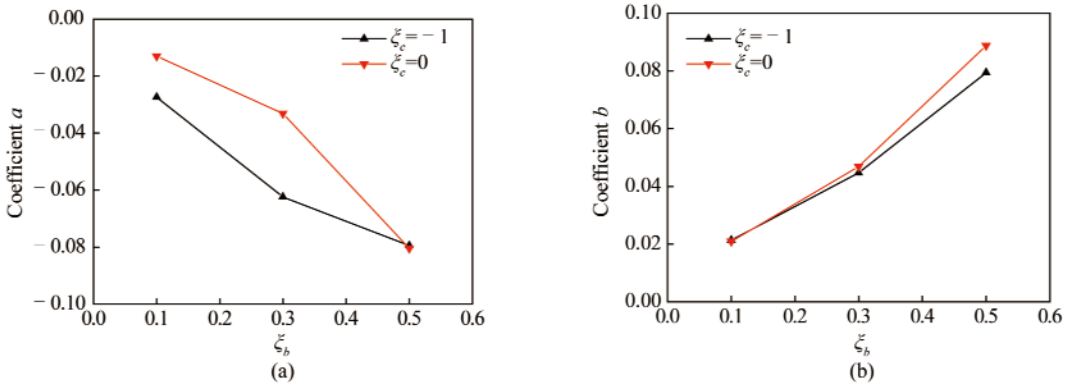

Fig. 11. Values of a and b under various ξ_b and ξ_c.

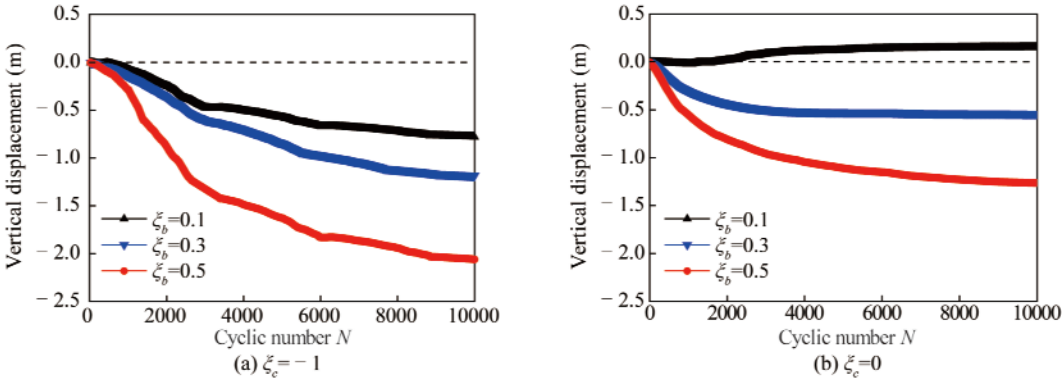

Fig. 12. Vertical displacement in relation to cycles under various ξ_b.

leads to a larger deformed soil range around the MSC, resulting in the larger settlement.

In addition, by comparing Fig. 12a with Fig. 12b, it shows that when the load amplitude is constant, the settlement of the MSC under two-way cyclic load (ξ_c=−1) is larger than that under one-way cyclic loading. The reason is that the sand shear strength decreases induced by the increasing of the deformed zone under two-way cyclic load. However, when $\xi_c = 0$, $\xi_b = 0.1$, the MSC is uplifted, as the soil inside and around the MSC undergoes dilatancy under cyclic loading.

Fig. 13 gives the range of the deformed soil under different combinations of ξ_b and ξ_c after 10000-cycle loading. It evidently shows that when the load amplitude is constant, the range of the deformed soil around the MSC under two-way cyclic load ($\xi_c = -1$) is greater than the range under unsymmetrical one-way cyclic load ($\xi_c = 0$). Besides, the scope of the deformed soil along horizontal and vertical direction becomes larger with the increasing load amplitude as expected.

5 Accumulated rotation of the MSC under combined wind and wave loads

Another major concern of designing OWT foundations is to address the effect of wind loading. As shown in Fig. 14, the wind load generally acts on the blades and tower of the OWT, and the resulting overturning moment will generate a significant impact on the stability of the

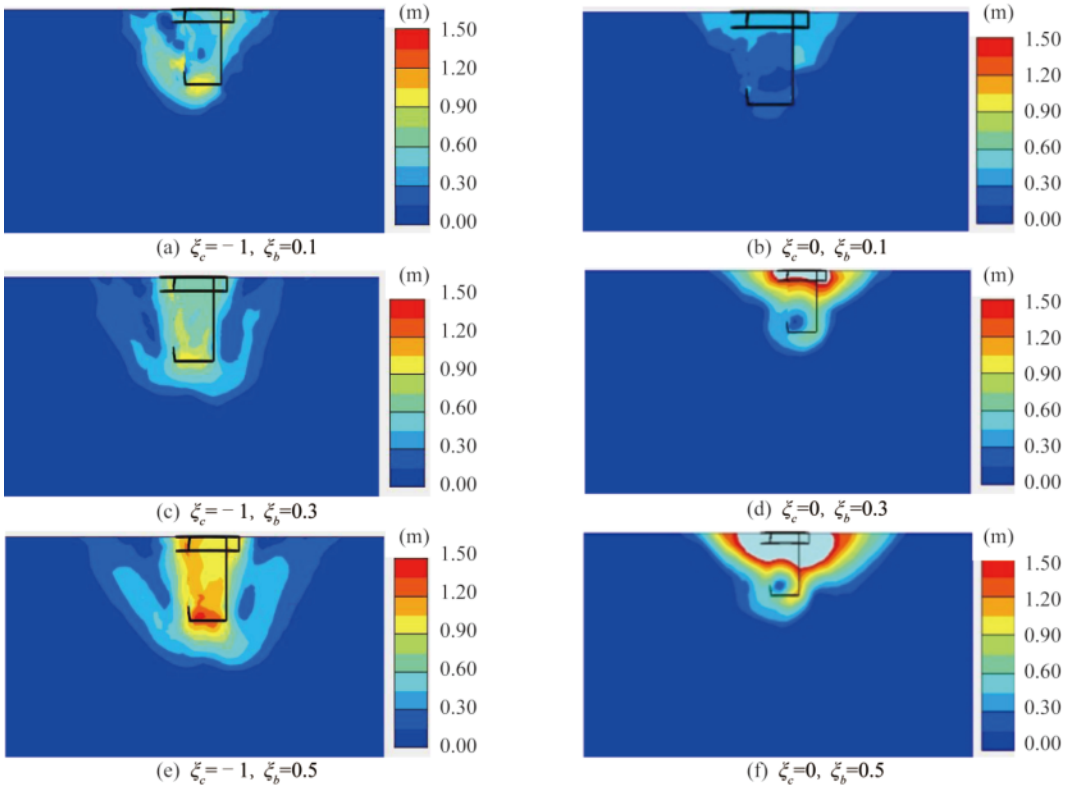

Fig. 13. Range of deformed soil under various wave load parameters.

foundation. In order to simplify calculation, the effect of wind load on the wave propagation was ignored, and the wave load and wind load were calculated separately. Arany et al. (2017) considered the wind thrust force (*Th*) acting on the wind turbine to be

$$Th = \frac{1}{2}\rho_a A_R C_T U^2, \tag{13}$$

where ρ_a is the air density, A_R is the rotor swept area determined by OWT's blade length, C_T is the thrust coefficient, wind velocity U is set to be 8.6 m/s according to practice engineering.

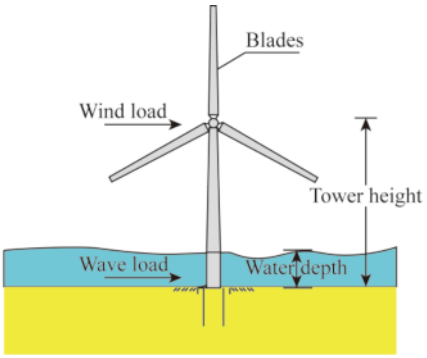

Fig. 14. Wind-driven generator model.

The accumulated rotation and vertical displacement of the MSC under combined wind and wave loads are shown in Fig. 15. The accumulated rotation-cyclic number curve of the MSC obtained under both wind and wave loads follows the same trend with that obtained under the wave load. The accumulated rotation of the MSC was mainly generated in the first 4000 cycles. And the vertical settlement tends to be stable gradually after 2000 cycles. In addition, the MSC generates greater accumulated rotation along the wind load direction than that under the wave loading, for the reason that the wind load acts on the blades resulting in large force and moment on the MSC. When the cyclic load number reaches a certain value, the accumulated rotation and the settlement no longer increase, and the MSC reaches a steady state.

The relationship between the accumulated rotation and cyclic number of the MSC under the combination of the wave and wind loads can be expressed as:

$$\Delta\theta(N) = -0.05 + 0.04 \lg N, \tag{14}$$

where a and b equal 0.05 and 0.04, respectively. As a result, it is feasible to provide reference for the prediction of the service life of the wind turbines.

6 Conclusions

This paper studies the response of the MSC under wave loading and its accumulated rotation under various load parameters of cyclic loading using numerical simulations. The following conclusions can be obtained:

(1) The MSC accumulated deformation under cyclic wave load decreases by 21% compared with the RSC, indicating that the MSC is capable for the OWT.

(2) The accumulated rotation of the MSC increases linearly with the logarithm of the loading cycle number. It has a significant increase in the first 4000 cycles, and then it becomes stable gradually.

(3) The scope of the deformed soil around the MSC under two-way cyclic load (ξ_c =−1) is larger than the range under one-way cyclic loading (ξ_c =0). It also increases as the cyclic load amplitude increases as expected. And an equation is proposed to predict rotation under cyclic wave loading.

(4) The MSC has a larger accumulated rotation under combined wind and wave loads compared with the accumulated rotation under wave load. The equation proposed is reliable to predict the accumulated rotation under this loading condition.

In this study, the wave load and wind load are determined separately in the simplified method. The wave load is regarded as a regular cyclic load and the influence of the wind on the wave propagation is ignored. But in actual engineering, the wind load is a dynamic load and it strongly influences the evolution of waves. Further work would be carried out to consider the influence of the wind on the wave propagation through the sea state parameters such as

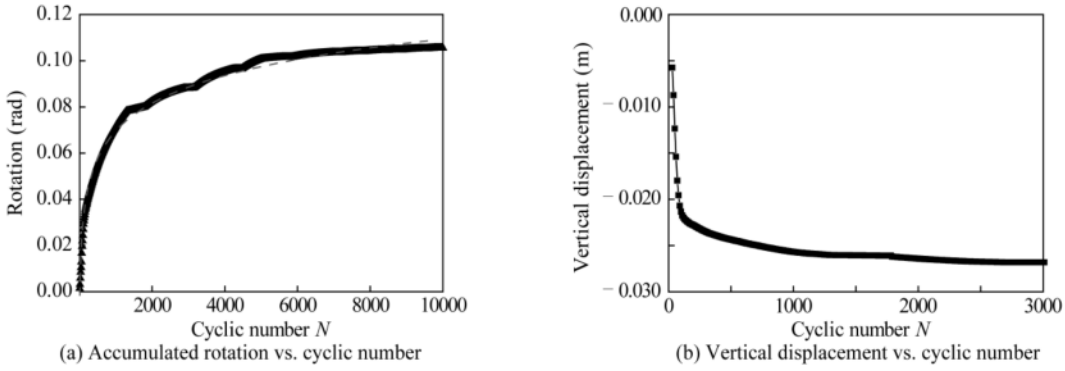

Fig. 15. Displacement of the MSC under combined wave and wind load.

the wind velocity and water depth, and the bearing behavior of the MSC under extreme conditions, especially the 50-year extreme wave load should also be taken into account.

References

Arany, L., Bhattacharya, S., Macdonald, J. and Hogan, S.J., 2017. Design of monopiles for offshore wind turbines in 10 steps, *Soil Dynamics and Earthquake Engineering*, 92, 126–152.

Awad-Allah, M.F., Yasufuku, N. and Abdel-Rahman, A.H., 2017. Cyclic response of wind turbine on piles in unsaturated sand, *International Journal of Physical Modelling in Geotechnics*, 17(3), 161–176.

China Classification Society, 2005. *Rules for Construction and Classification of Mobile Offshore Drilling Units*, China Communications Press, Beijing. (in Chinese)

Dean, E.T., 2010. *Offshore Geotechnical Engineering: Principles and Practice*, Thomas Telford, London.

Galavi, V., Petalas, A. and Brinkgreve, R.B.J., 2013. Finite element modelling of seismic liquefaction in soils, *Geotechnical Engineering Journal of the SEAGS & AGSSEA*, 44(3), 55–64.

Hydropower and Water Resources Planning and Design General Institute, Ministry of Water Resources of China, 2008. *Design Regulations on Subgrade and Foundation for Wind Turbine Generator System*, FD003-2007, China Water Power Press, Beijing. (in Chinese)

Ibsen, L.B. and Brincker, R., 2004. Design of a new foundation for offshore wind turbines, *Proceedings of the 22nd International Modal Analysis Conference* (*IMAC*), Detroit, Michigan, USA.

Ju, L., Vassalos, D. and Boulougouris, E., 2016. Numerical assessment of cargo liquefaction potential, *Ocean Engineering*, 120, 383–388.

Leblanc, C., Houlsby, G.T. and Byrne, B.W., 2010. Response of stiff piles in sand to long-term cyclic lateral loading, *Géotechnique*, 60(2), 79–90.

Li, D.Y., Qi, Y.S., and Zhang, Y.K., 2017. Numerical modelling of bearing capacities of skirted suction caissons under combined loads, *Journal of Guangxi University* (*Natural Science Edition*), 42(4), 1369–1377. (in Chinese)

Li, D.Y., Zhang, Y.K., Feng, L.Y. and Gao, Y.F., 2015. Capacity of modified suction caissons in marine sand under static horizontal loading, *Ocean Engineering*, 102, 1–16.

Liu, J.W., Duan, N., Cui, L. and Zhu, N., 2019. DEM investigation of installation responses of jacked open-ended piles, *Acta Geotechnica*, 14(6), 1805–1819.

Morison, J.R., Johnson, J.W. and Schaaf, S.A., 1950. The force exerted by surface waves on piles, *Journal of Petroleum Technology*, 2(5), 149–154.

Nielsen, S.D., Ibsen, L.B. and Nielsen, B.N., 2017. Response of cyclic-loaded bucket foundations in saturated dense sand, *Journal of Geotechnical and Geoenvironmental Engineering*, 143(11), 04017086.

Nikitas, G., Vimalan, N.J. and Bhattacharya, S., 2016. An innovative cyclic loading device to study long term performance of offshore wind turbines, *Soil Dynamics and Earthquake Engineering*, 82, 154–160.

Senders, M., 2009. *Suction Caissons in Sand as Tripod Foundations for Offshore Wind Turbines*, Ph.D. Thesis, University of Western Australia, Perth.

Tsegaye, A.B., 2010. *Plaxis Liquefaction Model* (*UBC3D*), Technical Report, Plaxis B.V., Delft.

Wobbes, E., Beuth, L., Vuik, C. and Stolle, D., 2017. Modeling of liquefaction using two-phase FEM with UBC3D-PLM model, *Procedia Engineering*, 175, 349–356.

Yang, M., Luo, R.P. and Li, W.C., 2018. Numerical study on accumulated deformation of laterally loaded monopiles used by offshore wind turbine, *Bulletin of Engineering Geology and the Environment*, 77(3), 911–921.

Zhang, Y.K., Li, D.Y. and Gao, Y.F., 2016. Earth pressures on modified suction caisson in saturated sand under monotonic lateral loading, *Journal of Renewable and Sustainable Energy*, 8(5), 053312.

Zhu, B., Byrne, B.W. and Houlsby, G.T., 2013. Long-term lateral cyclic response of suction caisson foundations in sand, *Journal of Geotechnical and Geoenvironmental Engineering*, 139(1), 73–83.